Materials Chemistry and Physics 337 (2025) 130455

Contents lists available at ScienceDirect

Materials Chemistry and Physics

journal homepage: www.elsevier.com/locate/matchemphys

Effect of processing temperature on performance of screen-printed graphite electrodes

Barbara Repič [a,b], Kristian Radan [a], Gregor Marolt [c], Andreja Benčan Golob [a], Danjela Kuscer [a,b,*]

[a] Jožef Stefan Institute, Jamova cesta 39, Ljubljana, Slovenia
[b] Jožef Stefan International Postgraduate School, Jamova cesta 39, Ljubljana, Slovenia
[c] University of Ljubljana, Faculty of Chemistry and Chemical Technology, Večna pot 113, Ljubljana, Slovenia

HIGHLIGHTS

- Electrochemical response of screen-printed graphite films is tailored using the processing temperature.
- Graphite undergoes fragmentation due to decomposition of the organic phase.
- Graphene layers order above 650 °C.
- Ordering of graphite films enhances the electrical conductivity and electrochemical response.

GRAPHICAL ABSTRACT

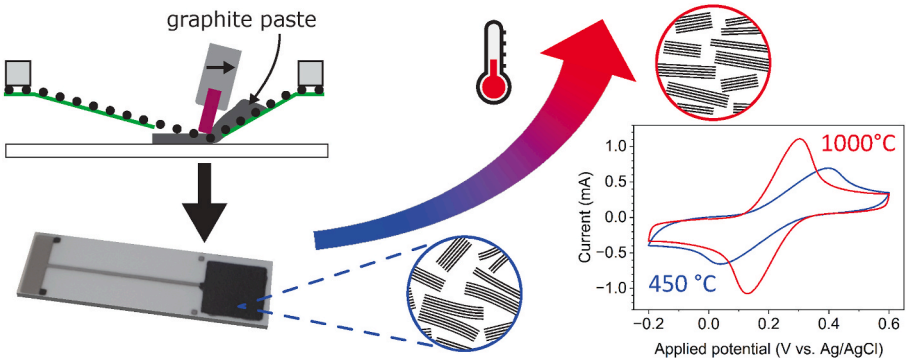

ARTICLE INFO

Keywords:
Screen-printed electrodes
Graphite
Thick films
Cyclic voltammetry
Electrochemistry
Processing

ABSTRACT

Graphite thick films have been considered as an effective integrated working electrode in disposable electrochemical sensors for the on-site detection of pollutants in remote locations. The processing conditions of graphite thick films are not well documented, which hinders progress in their use. By combining profilometry, optical microscopy, X-ray powder diffraction, and Raman spectroscopy, we show that the structural development of graphite thick films strongly depends on the processing temperature. After thermal annealing of the screen-printed paste, the arrangement of the graphene layers improved and the organic components from the paste facilitated the fragmentation of the graphite grains. The resulting sheet resistance of the thick films decreases and contributes to a higher electron-transfer rate and thus to faster redox processes at the electrode surface. The elucidation of the relationship between processing and properties offers new opportunities to customise the properties of graphite thick films for a variety of applications requiring defect engineering.

* Corresponding author. Jožef Stefan Institute, Jamova cesta 39, Ljubljana, Slovenia.
E-mail address: danjela.kuscer@ijs.si (D. Kuscer).

https://doi.org/10.1016/j.matchemphys.2025.130455
Received 2 October 2024; Received in revised form 10 January 2025; Accepted 24 January 2025
Available online 28 January 2025

1. Introduction

Disposable electrodes made by thick-film technology enable the miniaturisation of electrochemical sensors and the on-site detection of pollutants at remote locations with good selectivity and sensitivity [1–4]. The demand for the efficient monitoring of emerging pollutants in the environment and food requires disposable electrodes that allow a rapid and selective analysis, can be adapted to different analytical requirements, and take into account the complexity and compatibility of the analytes [4]. Thick-film technology is well established, and the so-called screen-printed electrodes, composed of working (WE), (quasi-)reference (RE) and counter (CE) electrodes together with electrical interconnections integrated onto a substrate, are commercially available. The RE is usually made from Ag or a mixture of Ag and AgCl, while CE and WE are made from metals such as silver, platinum and gold or from carbon-based materials. The WE is an important component of the disposable device, since the materials of the WE affect the kinetics and thermodynamics of the electron-transfer reactions. The processes at the electrode surface depend on each specific reaction, are complex, and often insufficiently understood. Therefore, the WE materials are frequently selected empirically. A pristine WE has often been modified with nanomaterials and/or biomolecules to improve the analytical signal, and thus the efficiency of the reactions, selectivity and sensitivity [5]. However, the analytical reproducibility of modified electrodes is uncertain and difficult to control and remains the main limitation for their use [6]. It is, therefore, necessary that the analytical signal is already large in the pristine WE.

Carbon-based materials are already well established and applied in WEs as they offer a large specific surface area, a high electrical conductivity, a wide electrochemical window for the electrochemical detection of various analytes and a low cost. Graphite is a unique and important material for the electrochemical detection of organic compounds, thus it is frequently used for processing pristine screen-printed WE. The first step includes the preparation of a paste for screen printing, which comprises the dispersion of graphite particles in an organic vehicle and adjusting its rheological properties to the screen-printing technology. The paste is then deposited onto the substrate, dried and heated at an elevated temperature to remove the organic vehicle and develop the desired microstructure and functional response [7,8]. For carbon-based materials, the post-annealing step of the as-deposited layers is of paramount importance. It must be performed in an oxygen-free atmosphere using the optimal temperature regime to prevent the oxidation and the decomposition of the material as well as the delamination of the thick film from the substrate. In thick-film processing, the adhesion of the material to the substrate may not be sufficient due to the thermal expansion mismatch between the carbon-based material and the substrate. In particular, graphite consists of carbon atoms arranged in layers in a hexagonal crystal structure with a distance between the planes of ~0.335 nm and with an in-plane interatomic distance of 0.142 nm [9,10]. This unique, layered structure results in anisotropic properties. For example, its thermal expansion coefficient (TEC) originates from very distinct bonding interactions between the carbon atoms in this crystal structure. In the temperature range from room temperature to ~400 °C, the TEC parallel to the c-axis (out-of-plane) of the hexagonal lattice is large and positive, while parallel to the basal planes (in-plane) it is relatively small and even negative. For example, upon heating to 225 °C, the graphite is expanding out-of-plane (TEC of $20 \times 10^{-6}\,K^{-1}$), while it shrinks parallel to the basal planes (TEC of $1-2 \times 10^{-6}\,K^{-1}$) [11,12]. These values are different than those of an alumina substrate with an isotropic TEC of $8.1 \times 10^{-6}\,K^{-1}$. To minimise the formation of defects and prevent delamination of the graphite from the alumina, the processing conditions such as the as-deposited layer thickness, processing temperature, time, heating and cooling rates must be precisely controlled. The electrical conductivity of graphite is also anisotropic. It is significantly larger in the in-plane than the out-of-plane direction because of the delocalised electrons between the graphite layers. The electrical conductivity of the graphite, however, depends on many parameters, such as the thermal annealing, density and particle size of the material, as well as the number of adjacent graphite layers, their orientation and the contact resistance between them [12–14].

The widespread use of graphite in advanced devices, including electrochemical sensors, results in an investigation of the graphite-powder targeting to improve selected properties with the processing conditions. This includes, for example, improving the electrical properties using techniques such as exfoliation [15]. Numerous studies have reported the modification and/or functionalisation of commercial, integrated graphite working electrodes with nanomaterials [16–18], but little is known about the processing of thick-film, pristine graphite electrodes. A better understanding of the processing of the screen-printed electrode would also lead to better reproducibility of this type of electrodes. Reproducibility is an issue and presents a key challenge for the widespread and long-term application of disposable electrochemical sensors.

Here, we report on the pristine graphite thick films on alumina processed by screen printing and subsequent heating at elevated temperatures in a controlled argon atmosphere. We focus on the effect of annealing of graphite thick films at different temperatures on the thickness, roughness, crystal and defect structure and their sheet resistance. We relate these properties of the graphite thick films to their electrochemical response in a model fluid. We demonstrate the ability to tailor the electrochemical response of graphite thick films by processing temperature in a reproducible and simple manner, thus extending their application as reliable working electrodes in disposable electrochemical sensors.

2. Experimental

The graphite thick films were prepared from graphite powder (graphite flake, 99.8 %, Alfa Aesar, Karlsruhe, Germany) dispersed in an organic vehicle, consisting of 60 wt% α-terpineol, 25 wt% [2−(2−butoxyetoxy)ethyl] acetate and 15 wt% ethyl cellulose. Graphite powder exhibits a log-normal particle size distribution with a median particle size of 15 μm (Fig. S1). The paste with 15 vol% of powder was screen printed on alumina (96 % Al_2O_3, Rubalit 708S, CeramTec) with a screen printer (P-250AVF, KEKO Equipment, Žužemberk, Slovenia), as a square with sides of 8 mm. Geometrical area of the graphite thick film WE is therefore 0.64 cm^2. A stainless steel mesh with 200 openings per inch was used for the screen printing. Two layers were deposited, and each layer was dried at 120 °C for 15 min in air. Based on the TG analysis of the paste (Fig. S2), the samples were subsequently fired in a tube furnace at 450 °C for 1 h with a heating rate of 2 K min^{-1}, or further heated to 650, 850 or 1000 °C for 30 min with a heating rate of 5 K min^{-1} and then cooled to room temperature with cooling rate of 5 K min^{-1} in an argon atmosphere. During the annealing process the oxygen content at the outlet was monitored with an oxygen analyser (Rapidox 2100-Z, Cambridge Sensotec, UK). The resulting samples are denoted as G_450, G_650, G_850 and G_1000, respectively.

The thickness of the films was measured using a contact stylus profilometer (DektakXT Advanced System, Bruker, Billerica, MA, USA). From the measurements the root-mean-square surface roughness (R_q) was determined after high-pass filtering of the profile using Gaussian regression with a cut-off wavelength of 0.8 mm.

The sheet resistance (R_s) of the films was measured using a four-point probe technique and a high-voltage source-measure unit (SMU, Keithley 237, Cleveland, Ohio, USA) [19]. A geometric correction factor of 0.795 was used for the calculation of R_s. Details of experimental setup and used equation are given in Supplementary information.

The X-ray powder diffraction (XRD) patterns were collected at room temperature in the 2θ range from 20° to 60° with a step of 0.01° and 0.12 s/step using Benchtop Powder X-Ray Diffractometer (MiniFlex 600-C, Rigaku, Tokyo, Japan). The phases were identified using X'Pert HighScore Plus 3.0e (PANalytical) and the PDF−4+/Web 2022 database. The number of graphite layers (N) was calculated by dividing the crystallite size in the out-of-plane direction (L_c) by the interlayer spacing (d) of the (002) diffraction peak. The value of L_c was calculated using

equation [20] $L_c = \frac{K\lambda}{FWHM \cos\theta}$, where λ is the X-ray wavelength of 0.154 nm; K is the shape factor of 1; θ is the Bragg angle of the 002 diffraction peak and FWHM is its full width at half maximum.

Room-temperature Raman spectra were measured on a dispersive Raman spectrometer (Senterra II, Bruker, Billerica, Massachusetts, USA) equipped with a confocal microscope (Olympus BX53 M, Olympus Corporation, Tokyo, Japan SA). A 532-nm excitation line at 5 mW was focused on the samples through a 50× long-working-distance microscope objective (N.A. 0.5). Spot measurements with 50 scans and a 1 s integration time were collected over a 50–4250 cm^{-1} spectral range with a resolution of 4 cm^{-1}. Measurements on 15–20 different spots for each sample were averaged, baseline corrected and normalized. Bruker's OPUS software was used for the data acquisition and the spectral pre- and post-processing.

Electrochemical measurements were performed in a 50 mL electrochemical cell using Ag/AgCl RE, platinum sheet CE (both from Metrohm), and G_450, G_650, G_850 and G_1000 as the WE. Prior to the measurements of the graphite thick films, the electrical contacts were made from a colloidal silver paste (Ted Pella Inc, Redding, California, US), dried at room temperature and covered with a nitrocellulose-based coating to prevent their contacts with water solutions. Cyclic voltammograms (CVs) were measured using potentiostat-galvanostat (Multi Autolab M 204, Metrohm, The Netherlands) controlled by Nova 2.1.5 software. The measurements were performed at 25 °C between −0.2 V and +0.6 V, starting at 0.0 V in an initial positive scan with a potential step of 2.44 mV using different scan rates of 20, 30, 40, 50 and 100 mV s^{-1} for films annealed at 1000 and 850 °C and 2, 5, 7, 10, 15 and 100 mV s^{-1} for films annealed at 650 and 450 °C, respectively.

The samples were characterised in a 0.1 M phosphate buffer solution (PBS) at pH = 7. The PBS was prepared from NaH_2PO_4 (99.0 %) and Na_2HPO_4 (>99.0 %), both from Merck, Darmstadt, Germany, dissolved in ultrapure water (resistivity ≥18 MΩ cm). The electrochemical responses of the samples were also measured in 5 mM hexacyanoferrate PBS solution (HCF) with an equimolar concentration of Fe^{2+}/Fe^{3+} prepared from $K_4[Fe(CN)_6]\bullet 3H_2O$ (≥98.5 %) and $K_3[Fe(CN)_6]$ (99 %), both from Carlo Erba, Val-de-Reuil, France.

3. Results and discussion

The graphite thick films on alumina substrates were fired at 450, 650, 850 and 1000 °C in an argon atmosphere (denoted as G_450, G_650, G_850 and G_1000, respectively). Due to the inert atmosphere with an oxygen content below 5 ppm during the whole annealing process, the degradation of the samples was negligible. All the samples had similar thicknesses, a uniform surface and were well adhered to the substrate. The average values and standard deviations of the thick-film thickness, surface roughness and sheet resistance measured on 8 samples prepared at each processing temperature (T_p) are listed in Table 1. The representative images of the surface of the G_450, G_650, G_850 and G_1000 by optical microscopy are shown in Fig. S3.

Table 1
Thickness (t), surface roughness (R_q) and sheet resistance (R_s) of graphite thick films on alumina fired at different T_p in argon atmosphere (N = 8).

Sample	t [μm]	R_q [μm]	R_s [Ω/sq]
G_450	39.0 ± 1.9	4.2 ± 0.8	122.2 ± 5.6
G_650	39.2 ± 1.0	4.2 ± 0.4	65.7 ± 4.4
G_850	39.2 ± 1.5	4.1 ± 0.5	8.7 ± 1.0
G_1000	39.1 ± 1.9	4.2 ± 0.7	7.2 ± 1.1

The XRD diffraction patterns of G_450, G_650, G_850 and G_1000 are shown in Fig. 1a. The diffraction peaks at ~26° and ~55° belong to graphite with a hexagonal crystal structure (PDF 00-56-0159). Additionally, we observed diffraction peaks originating from the alumina substrate (PDF 00-010-0173), which are associated with the X-ray penetration depth in the graphite. X-rays can penetrate several hundreds of micrometres into the graphite, a distance much greater than the thickness of the graphite layer, i.e., ~30 μm. Therefore, the signal from the alumina substrate cannot be disregarded in the graphite films reported here. By analysing the position and width of the 002 diffraction peak of graphite, we determined the crystallite size L_c and the corresponding number of carbon layers. For all the samples, the maximum of the 002 diffraction peak was consistently found at a d-spacing of 0.335 nm. However, the intensity and FWHM of the 002 diffraction peak showed opposite trends with increasing T_p. As the temperature rose, the intensity increased while the FWHM decreased, which implies an increase in the crystallinity. This can be interpreted as an increase in the volume fraction of the well-ordered graphite phase with increasing T_p, which corresponds to an increase in L_c (002) and the number of graphene layers in graphite thick films (Fig. 1b). These results indicate that upon heating the graphite thick films, the structure of the graphite is better ordered, but partially fragmented. Previous reports suggest that introducing inorganic molecules between the graphite layers can cause the layers to expand, separate, and exfoliate [21]. In this study, we screen printed the graphite paste composed of graphite flakes, terpineol, butoxy-ethoxy-ethyl acetate and ethyl cellulose. Thermal analyses revealed that the organic additives were removed from the paste up to ~450 °C in an argon atmosphere [22]. Thus, during the heating of the screen-printed layers up to 450 °C in argon, the organic components decompose and can probably penetrate between the layers of graphite, allowing the fragmentation of the graphite [23,24].

To test this hypothesis, we compared the crystallite size and the number of graphene layers in the as-received graphite powder, and in the graphite powder heated to 850 °C in argon. Surprisingly, the L_c (200) and the number of layers were similar for both powders, ~45 nm and ~130. However, when examining the graphite thick films processed at the same temperature of 850 °C, G_850, the L_c (200) and the number of layers were much larger, 88 nm and 262, respectively (Fig. 1b). This suggests that the organic components in the paste play a key role in more efficient ordering and fragmentation of the graphite at elevated temperatures. An improvement in the ordering has also been observed in

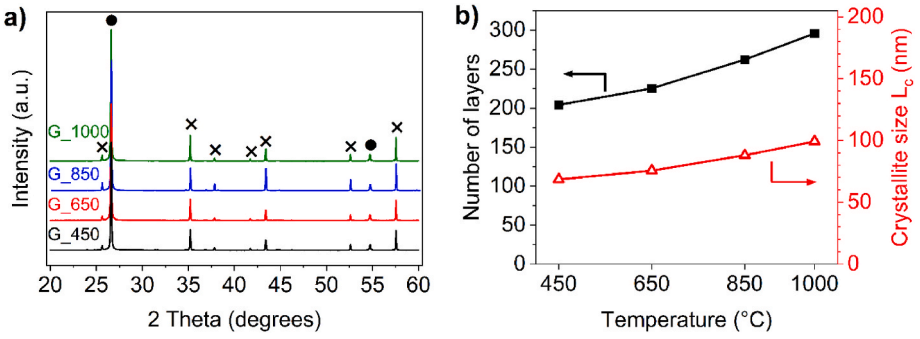

Fig. 1. a) XRD patterns of G_450, G_650, G_850 and G_1000 (●: graphite, ×: Al_2O_3). b) Number of graphene layers and out-of-plane crystallite size L_c (002) in graphite thick films as a function of temperature.

other carbon-based samples and attributed to the presence of organic compounds, such as ethanol or ethylene. These compounds decompose upon heating and contribute to the effective restoration of the graphene's structure and the higher electrical conductivity of the material [23,24].

The temperature-induced changes in the graphite structure, the bonds and the degree of disorder were investigated by Raman spectroscopy. The Raman spectra of the as-received graphite powder and the graphite powder heated to 850 °C, collected at room temperature, are shown in Fig. S4. Both spectra are similar and show characteristic features of disordered graphite [25], which remain essentially unaffected by the thermal treatment. On the other hand, the representative Raman measurements of the G_450, G_650, G_850 and G_1000 thick films, shown in Fig. 2a,b, exhibit spectral differences.

The Raman spectra of all the analysed thick films and graphite powders are dominated by three well-defined bands found at characteristic wavenumber positions (for visible excitation) of the graphitic materials [9,10,25,26], i.e., the D band at ~1350 cm^{-1}, the G band at ~1560 cm^{-1} and the 2D band at ~2700 cm^{-1}. The G band is Raman active for all sp^2 carbon networks and represents the in-plane stretching vibration of the sp^2 carbon bonds, both in rings and chains. The D peak is a disorder-induced band that has been assigned to the breathing modes of the sp^2 atoms in the rings and does not occur in defect-free graphite samples [9,27–29]. In contrast to the D band, its second-order overtone, the 2D mode, is always allowed (hence it is often referred to as G') and no defects are required for its activation.

The extent of the defects and disorder in the samples can be estimated from the intensity ratio of the D and G bands, I_D/I_G [30,31]. The largest I_D/I_G values (Fig. 2c) of 0.18 and 0.20 are observed for G_450 and G_650, respectively, which also have the D′ band at ~1600 cm^{-1} as a shoulder on the high frequency side of the G peak. These features indicate the highest degree of disorder in the thick films mentioned above [27,32,33]. The I_D/I_G ratio and the full width at half maximum (FWHM) of the G band (Fig. 2c) decrease with a further increase in T_p, while the D' shoulder gradually disappears. These results indicate a larger phase order and/or a reduction in the number of defects at temperatures above 650 °C [29,34]. The arrangement of the (002) planes in G_450 and G_850 can indeed be seen in the TEM images (Fig. S5), confirming improved alignment of (002) planes at higher temperatures.

Moreover, the average in-plane crystallite size (L_a) of the thick films, estimated according to the modified Tuinstra-Koenig relation $L_a = (2.4 \times 10^{-10})\lambda_l^4 \left(\frac{I_d}{I_g}\right)^{-1}$, where λ_l is the laser wavelength in nm units [9,27,35], increased at temperatures above 650 °C, rising from 94 nm to 150 nm for G_450 and G_1000, respectively (Fig. 2c). Similarly, the out-of-plane crystallite size (L_c), as determined by the X-ray diffraction (XRD) analysis, also showed an increase with higher T_p (Fig. 1b).

A presentation of the graphite thick films as a function of T_p is schematically shown in Fig. 3. In the as-deposited, unannealed thick

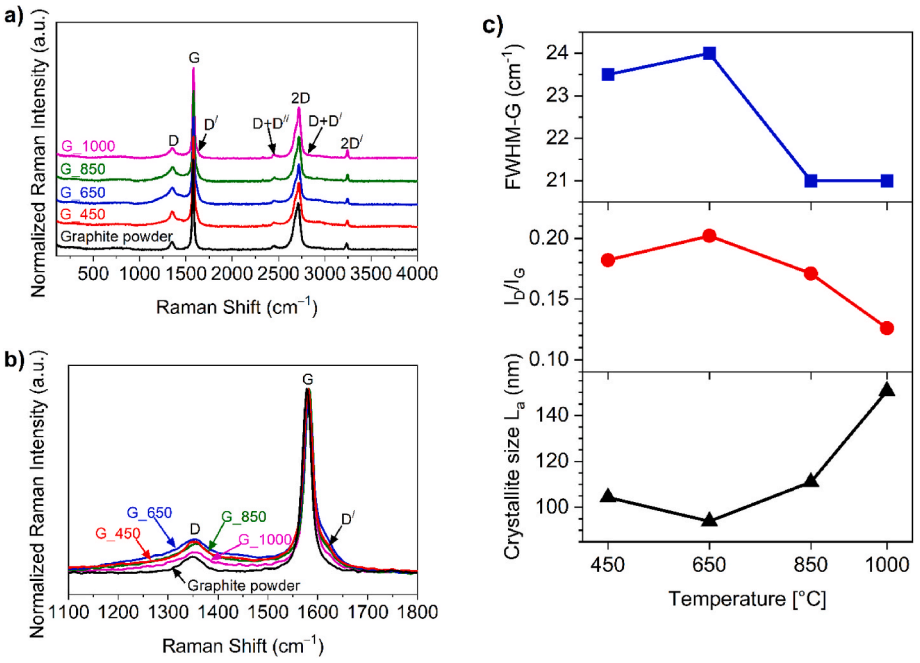

Fig. 2. Normalized Raman spectra of G_450, G_650, G_850 and G_1000 and as-received graphite powder a) full spectral range, b) the magnification of the 1100–1800 cm^{-1} spectral region; c) FWHM of the G band, I_D/I_G ratio and L_a as a function of temperature.

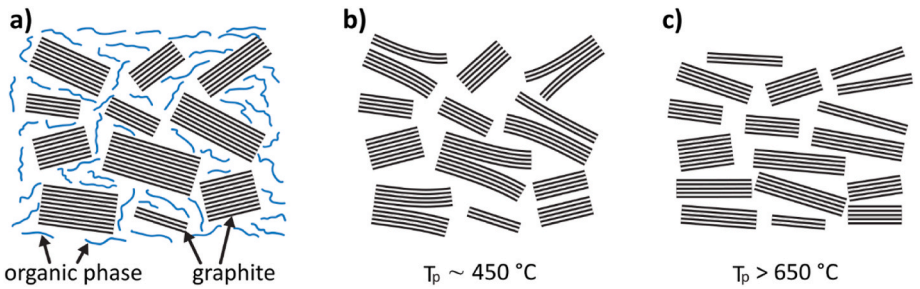

Fig. 3. Schematic presentation of graphite thick film. a) graphite paste for screen printing, b) fragmented graphite thick film at ~450 °C, c) ordered graphite thick film above 650 °C.

film, the graphite powder with randomly orientated grains is dispersed in an organic phase (Fig. 3a). When heated to 450 °C, the organic phase decomposes and the resulting products penetrate both between the graphite grains and between the interconnected graphene layers of the graphite structure. In the graphite structure, the connections between the graphene layers become weaker and lead to a partial separation of the layers. The resulting graphite thus consists of a disordered, twisted stack of graphene layers (Fig. S5b), while the graphite grains in the thick layer are still randomly orientated (Fig. 3b). This is reflected in a locally less ordered structure compared to that of the graphite powder (Fig. 2), and a larger crystallite size in the c-direction (L_c) (Fig. 1). As the temperature increases further, the graphite structure becomes more ordered. The graphene layers are ordered in the a-b direction (Fig. S5d), which is reflected in an increase of L_a (Fig. 2), and in the c-direction reflected in a larger L_c (Fig. 3c). Consequently, the ordering in the c-direction leads to an apparent increase in the number of graphene layers. We assume that the graphite partially fragments up to 450 °C when the organic phase decomposes, after which it remains constant. The ordering of the graphene within the graphite stack influences the electrical conductivity. The more ordered the structure is, the better it conducts electricity (Table 1).

The concerted contribution of all these parameters, although they have opposite effects on the electrical conductivity, led to a decrease in the sheet resistance of the graphite thick films with increasing T_p. It is known that the electrical conductivity of graphite is high along its basal planes, 500–1700 S cm^{-1}, and lower in the out-of-plane direction, 3–25 S cm^{-1}. The high in-plane electrical conductivity is related to the sp^2 hybridized carbon atoms, which enable high electron mobility, while weak interlayer interactions in the out-of-plane direction limit their mobility [12,36]. The electrical conductivity of graphite has also shown to be affected by the microstructure of the layer, including the grain size, density and impurities. The graphite grains are highly anisotropic and their orientation, distance and the contact between them affect the electrical conductivity of the layer. However, in this study all the thick films were processed from identical powder and paste with identical solids loading. Since the thickness and the roughness of all the studied graphite thick films were similar, we assume that the density of the layer did not vary significantly with T_p. Also, the grain size and the contact between the grains were similar for all the samples, as is evident from the optical microscopy images (Fig. S3). These findings suggest that the magnitude of the electrical conductivity of graphite thick films depends greatly on their local structure. Presumably, the graphite consists of well-ordered graphene layers separated by disordered regions at low T_p. With the increasing T_p the structure still contains the disordered regions but in lower amounts, the number of graphene layers increases (Fig. 1, Fig. S5). This facilitates more effective electron mobility and thus contributes to the higher electrical conductivity of the graphite thick films. Our results clearly indicate that the electrical conductivity of graphite thick films is correlated with the organic phase in the screen-printed paste and T_p, which both have an important effect on the resulting structure of the graphite.

The T_p of the graphite thick films is also reflected in their electrochemical response. Fig. 4a shows CVs of the background 0.1 M PBS with a pH of 7 and of 5 mM HCF measured at a scan rate of 0.1 V/s at 25 °C using the G_450, G_650, G_850, and G_1000 as WE. The average values and standard deviations of the electrochemical parameters determined for graphite thick-films prepared at each T_p are listed in Table 2. The absence of peaks in the recorded potential range in PBS (dashed lines) suggests that no species undergo oxidation or reduction on these electrodes, and neither does the electrode material itself within the scanned potential window. The capacitive currents show no significant trend with T_p and appear to be similar within the uncertainty. In HCF, the reduction and oxidation peaks at ~0.15 V and ~0.3 V, respectively, are well defined, but the cathodic and anodic peak currents (i_{pc}, i_{pa}) and the peak-to-peak separation (ΔE_p) were affected by the T_p between 450 and 850 °C, while similar values were measured for 850 and 1000 °C (Fig. 4b). The absolute values of i_{pc} and i_{pa} increased with the increasing T_p; however, their ratio, i_{pc}/i_{pa}, did not vary significantly with T_p and was close to unity for all the samples. It is also evident that ΔE_p decreases with increasing T_p, while the half-wave potential ($E_{1/2}$) is similar for all the samples. The decrease in ΔE_p is consistent with the decrease in the uncompensated resistance (R_u) determined with a positive-feedback method. The OCP values obtained in the presence of HCF were ~205 mV vs Ag/AgCl for all investigated electrode materials. When the potential is recalculated to the normal hydrogen electrode (NHE, E^0(Ag/AgCl/3 M KCl) = 0.209 V vs NHE [37]), the obtained potential of 0.414 V vs NHE correlates well with the values reported by O'Reilly et al. [38]. The OCP values are in good agreement with the CVs in Fig. 4 as they are aligned close to the values of half-wave potential in all cases, confirming

Table 2
Dependence of selected electrochemical parameters on T_p for the G_450, G_650, G_850 and G_1000.

	G_450	G_650	G_850	G_1000
OCP [mV] in PBS	81 ± 27	84 ± 9	73 ± 26	87 ± 18
OCP [mV] in HCF	210 ± 5	202 ± 8	205 ± 2	213 ± 3
R_u [Ω] in PBS	116.7 ± 44.6	90.3 ± 17.2	46.8 ± 5.6	41.0 ± 1.4
i_{pc}/i_{pa}	0.94 ± 0.01	0.96 ± 0.01	0.97 ± 0.01	0.95 ± 0.01
$\Delta E_{p\ [mV]}$	271 ± 78	275 ± 54	157 ± 17	167 ± 9
A_{ecsa} [cm^2]	1.14 ± 0.14	1.60 ± 0.14	2.20 ± 0.15	2.62 ± 0.05
k° [10^{-3} cm/s]	1.07 ± 0.16	1.62 ± 0.33	4.57 ± 0.71	5.31 ± 1.12

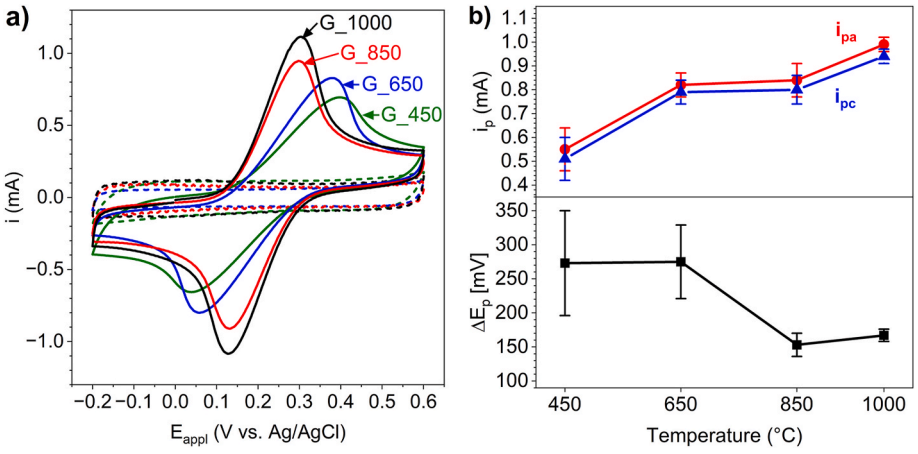

Fig. 4. Graphite thick film. a) CV curves of the PBS and HCF at G_450, G_650, G_850 and G_1000 measured at a scan rate of 0.1 V/s and at 25 °C. b) ΔE_p, cathodic (i_{pc}) and anodic (i_{pa}) peak currents as a function of T_p.

the potential is dictated by the $[Fe(CN)_6]^{3-/4-}$ redox couple according to the Nernst equation. On the other hand, the OCP values obtained in the absence of the redox couple were significantly lower, i.e., ~80 mV, and showed a higher standard deviation due to the lack of redox couple in the electrolyte. Therefore, the OCP values represent the so-called corrosion potential of the WE material itself in PBS, which is most likely controlled by the adsorbed oxygen (adsorbed during the electrode preparation) and/or the redox couple of carbon and carbon-oxygen species on the surface of the electrode materials [39]. No significant differences were found between OCP values of the studied WEs, indicating that the increasing annealing temperatures do not chemically affect the WE surface (e.g. oxidation etc.) but rather the ordering of the electrode material as discussed above.

The CVs of G_450, G_650, G_850, and G_1000 measured in HCF collected at different scan rates (ν) revealed that i_{pa} and i_{pc} increased and E_{pa} and E_{pc} shifted to more positive and negative potentials, respectively, with increasing ν. The absolute values of i_{pa} and i_{pc} increased linearly with the square root of ν over the investigated ν range for all the samples. The electroactive surface area (A_{ecsa}) was determined from the i_{pa} and the i_{pc} vs $\nu^{1/2}$ curve slope (Fig. S6) using Randles Ševčík equation for a quasi-reversible one-electron transfer process [40–42]. The electron-transfer rate constant k° was determined using the Nicholson method from the slope of the kinetic parameter ψ vs $\nu^{-1/2}$ curve (Fig. S7) [41,43]. Details about the equations and methods used for the calculation of A_{ecsa} and k° are described in Supplementary Information. It is evident that the electrochemically active surface area for the electrochemical reaction, A_{ecsa}, and the standard rate constant, k°, increased by a factor of 2.2 when T_p increased from 450 °C to 1000 °C (Table 2).

It seems that the most resistive thick film, G_450, possessed the smallest A_{ecsa}, the most sluggish electrochemical reaction and the largest ΔE_p, which suggests the largest ohmic resistance. All these parameters improved with a higher T_p, although we have not observed any significant changes in the thickness and surface roughness of the thick films. However, a more effective fragmentation of the graphite suggested by XRD and Raman spectroscopy, contributes to a higher electrical conductivity of the thick films. We, therefore, hypothesise that the electrical conductivity of the thick films plays an important role in their electrochemical response. Our results are consistent with a previous study, which showed that thermal annealing of the glassy carbon electrodes increases the electrical conductivity, decreases the ΔE_p and improves electrochemical reactivity [14]. Grennan et al. [44] also showed that higher annealing temperatures ranging between room temperature and 200 °C for the preparation of screen printed graphite-based WE using commercially available carbon paste resulted in a larger surface area, attributed to the decomposition of the polymeric binder. Compared to screen-printed graphite WEs (4 mm diameter) on a polyester substrate cured at 90 °C for 60 min in air [41], which exhibited A_{ecsa} of 0.0331 ± 0.0035 cm^2 and k° of $(0.401 \pm 0.022) \times 10^{-3}$ cm s^{-1}, the graphite thick films reported in this work demonstrate both a larger electroactive surface area (normalized with the geometric area) and faster electron transfer. Graphite thick films were also prepared from graphite powder at room temperature by aerosol-deposition and had a R_s of 27 Ω/sq [45]. Its electrochemical response in HCF, ΔE_p of 176 mV, A_{ecsa} of 1.94 cm^2 and k° of 1.9×10^{-3} cm s^{-1}, is higher than that of G_650 with an R_s of 65.7 ± 4.4 Ω/sq, but lower than that of G_850 with an R_s of 8.7 ± 1.0 Ω/sq. An alternative, reasonable explanation, draws on the difference between the electrochemical response of the unmodified and modified WEs. For example, Bottari et al. [46] reported that upon modification of the screen-printed graphite electrode with *o*-phenilenediamine, the peak current decreased and the ΔE_p increased with the number of cycles performed in HCF. This was assigned to the lower conductivity of the electrodes upon cycling, measured by electrochemical impedance spectroscopy (EIS). It is also known that the shape, size and chemical composition of the WE affect the mass transport, the thickness of the linear diffusion layer and thus the rate constant k° of the redox process. For sluggish processes, characterised by low k°, the concentration of the reactant at the electrode surface is not negligible. It is larger than those of the products, which might affect the mass transport of reactant towards the electrode [47]. Our experiments, performed with identical starting material and under identical conditions, but with WEs of different sheet resistances, imply the lowest k° value and thus the slowest electrode kinetics for T_p 450 °C. The k° values increase with T_p. These differences demonstrate the impact of the T_p of the graphite thick film on the electrochemical response.

4. Conclusions

We have demonstrated that the temperature annealing of screen-printed graphite thick films results in a decreased sheet resistance and improved electrochemical reactivity. After the thermal treatment of the screen-printed graphite layers at 450, 650, 850 and 1000 °C, we obtained ~40-μm-thick films, well adhered to an alumina substrate, with a surface roughness R_q of 4 μm, regardless of the processing temperature T_p. However, with increasing T_p the formation of additional graphene layers with a lower fraction of disorder regions could be related to the decomposition of organic phase in the screen-printed paste. When an organic phase is decomposed upon heating, the graphite partially fragmented. The fragmentation and ordering of the carbon atoms are essential for decreasing the sheet resistance of graphite thick films from 122 Ω/sq to 9.4 Ω/sq for the samples processed at 450 °C and 1000 °C, respectively. Lowering of the sheet resistance is also reflected in the improved electrochemical characteristics of the graphite thick films with larger cathodic and anodic peak currents, a smaller peak potential separation distance ΔE_p, a larger rate constant k° and thus a faster redox process. The elucidation of the relationship between the WE material processing and the properties offers new opportunities to customise the properties of graphite thick films for a variety of applications requiring defect engineering.

Declaration of generative AI and AI-assisted technologies in the writing process

The authors did not use generative AI and AI-assisted technologies in the writing process.

Funding

This work was supported by the Slovenian Research and Innovation Agency [grant numbers P2-0105, J2-3049, P1-0153, N1-0225]; Research Agency's Young Researchers Programme [grant numbers 56886 and PR-11483]; and Ministry of Higher Education, Science and Innovation of Republic Slovenia [grant number C3360-23-252004, M-ERA.NET].

CRediT authorship contribution statement

Barbara Repič: Writing – original draft, Visualization, Validation, Investigation, Formal analysis. **Kristian Radan:** Writing – original draft, Visualization, Resources, Investigation, Formal analysis. **Gregor Marolt:** Writing – review & editing, Validation, Supervision, Methodology. **Andreja Benčan Golob:** Validation, Investigation. **Danjela Kuscer:** Writing – review & editing, Writing – original draft, Visualization, Supervision, Resources, Project administration, Methodology, Investigation, Funding acquisition, Conceptualization.

Declaration of competing interest

The authors declare that they have no known competing financial interests or personal relationships that could have appeared to influence the work reported in this paper.

Acknowledgment

The authors thank Ivana Goričan and dr. Aadil Abass Shah for collecting the XRD patterns, and Nina Pugelj for performing selected electrochemical measurements. Katarina Žiberna is acknowledged for help with TEM analysis.

Appendix A. Supplementary data

Supplementary data to this article can be found online at https://doi.org/10.1016/j.matchemphys.2025.130455.

Data availability

Data will be made available on request.

References

[1] S. Cinti, D. Moscone, F. Arduini, Screen-printed electrodes as versatile electrochemical sensors and biosensors, in: 2017 IEEE East-West Des. Test Symp. EWDTS, 2017, pp. 1–4, https://doi.org/10.1109/EWDTS.2017.8110130.
[2] X. Liu, Y. Yao, Y. Ying, J. Ping, Recent advances in nanomaterial-enabled screen-printed electrochemical sensors for heavy metal detection, TrAC Trends Anal. Chem. 115 (2019) 187–202, https://doi.org/10.1016/j.trac.2019.03.021.
[3] A. García-Miranda Ferrari, S.J. Rowley-Neale, C.E. Banks, Screen-printed electrodes: transitioning the laboratory in-to-the field, Talanta Open 3 (2021) 100032, https://doi.org/10.1016/j.talo.2021.100032.
[4] R. Umapathi, S.M. Ghoreishian, S. Sonwal, G.M. Rani, Y.S. Huh, Portable electrochemical sensing methodologies for on-site detection of pesticide residues in fruits and vegetables, Coord. Chem. Rev. 453 (2022) 214305, https://doi.org/10.1016/j.ccr.2021.214305.
[5] A.M. Santos, M.H.A. Feitosa, A. Wong, O. Fatibello-Filho, M.D.P.T. Sotomayor, F. C. Moraes, Functionalized graphene, quantum dots, and PEDOT:PSS based screen-printed electrode for the endocrine disruptor bisphenol A determination, Sens. Actuators B Chem. 399 (2024) 134745, https://doi.org/10.1016/j.snb.2023.134745.
[6] J.P. Metters, E.P. Randviir, C.E. Banks, Screen-printed back-to-back electroanalytical sensors, Analyst 139 (2014) 5339–5349, https://doi.org/10.1039/C4AN01501K.
[7] D. Kuscer, Screen printing, in: M. Pomeroy (Ed.), Encycl. Mater. Tech. Ceram. Glas., Elsevier, Oxford, 2021, pp. 227–232, https://doi.org/10.1016/B978-0-12-803581-8.12082-X.
[8] M. Kosec, D. Kuscer, J. Holc, Processing of ferroelectric ceramic thick films, in: Multifunct. Polycryst. Ferroelectr. Mater., Springer Netherlands, Dordrecht, 2011, pp. 39–61, https://doi.org/10.1007/978-90-481-2875-4_2.
[9] F. Tuinstra, J.L. Koenig, Raman spectrum of graphite, J. Chem. Phys. 53 (1970) 1126–1130, https://doi.org/10.1063/1.1674108.
[10] S. Reich, C. Thomsen, Raman spectroscopy of graphite, Philos. Trans. R. Soc. Lond. Ser. Math. Phys. Eng. Sci. 362 (2004) 2271–2288, https://doi.org/10.1098/rsta.2004.1454.
[11] J.E. Zorzi, C.A. Perottoni, Thermal expansion of graphite revisited, Comput. Mater. Sci. 199 (2021) 110719, https://doi.org/10.1016/j.commatsci.2021.110719.
[12] M. Cermak, N. Perez, M. Collins, M. Bahrami, Material properties and structure of natural graphite sheet, Sci. Rep. 10 (2020) 18672, https://doi.org/10.1038/s41598-020-75393-y.
[13] S. Rattanaweeranon, P. Limsuwan, V. Thongpool, V. Piriyawong, P. Asanithi, Influence of bulk graphite density on electrical conductivity, Procedia Eng. 32 (2012) 1100–1106, https://doi.org/10.1016/j.proeng.2012.02.061.
[14] Y. Lim, J.H. Chu, D.H. Lee, S.-Y. Kwon, H. Shin, Increase in graphitization and electrical conductivity of glassy carbon nanowires by rapid thermal annealing, J. Alloys Compd. 702 (2017) 465–471, https://doi.org/10.1016/j.jallcom.2017.01.098.
[15] M. Cai, D. Thorpe, D.H. Adamson, H.C. Schniepp, Methods of graphite exfoliation, J. Mater. Chem. 22 (2012) 24992, https://doi.org/10.1039/c2jm34517j.
[16] G.M.E. Silva, D.F. Campos, J.A.T. Brasil, M. Tremblay, E.M. Mendiondo, F. Ghiglieno, Advances in technological Research for online and in situ water quality monitoring—a review, Sustainability 14 (2022) 5059, https://doi.org/10.3390/su14095059.
[17] K. Torres-Rivero, A. Florido, J. Bastos-Arrieta, Recent trends in the improvement of the electrochemical response of screen-printed electrodes by their modification with shaped metal nanoparticles, Sensors 21 (2021) 2596, https://doi.org/10.3390/s21082596.
[18] B. Pérez-Fernández, A. Costa-García, A. de la Escosura-Muñiz, Electrochemical (Bio)Sensors for pesticides detection using screen-printed electrodes, Biosensors 10 (2020) 32, https://doi.org/10.3390/bios10040032.
[19] D.K. Schroder, Semiconductor Material and Device Characterization, third ed., John Wiley & Sons, New York, 2005 https://doi.org/10.1002/0471749095.
[20] N. Iwashita, C.R. Park, H. Fujimoto, M. Shiraishi, M. Inagaki, Specification for a standard procedure of X-ray diffraction measurements on carbon materials, Carbon 42 (2004) 701–714, https://doi.org/10.1016/j.carbon.2004.02.008.
[21] A.M. Darabut, Y. Lobko, Y. Yakovlev, M.G. Rodríguez, K. Veltruská, B. Šmíd, P. Kúš, J. Nováková, M. Dopita, M. Vorokhta, V. Kopecký, M. Procházka, I. Matolínová, V. Matolín, Influence of thermal treatment on the structure and electrical conductivity of thermally expanded graphite, Adv. Powder Technol. 33 (2022) 103884, https://doi.org/10.1016/j.apt.2022.103884.
[22] B. Repič, G. Marolt, D. Kuscer, Carbon-based thick films for electrochemical detection of neonicotinoid insecticides, J. Electroanal. Chem. (2025).
[23] V. López, R.S. Sundaram, C. Gómez-Navarro, D. Olea, M. Burghard, J. Gómez-Herrero, F. Zamora, K. Kern, Chemical vapor deposition repair of graphene oxide: a route to highly-conductive graphene monolayers, Adv. Mater. 21 (2009) 4683–4686, https://doi.org/10.1002/adma.200901582.
[24] C. Gong, M. Acik, R.M. Abolfath, Y. Chabal, K. Cho, Graphitization of graphene oxide with ethanol during thermal reduction, J. Phys. Chem. C 116 (2012) 9969–9979, https://doi.org/10.1021/jp212584t.
[25] M.A. Pimenta, G. Dresselhaus, M.S. Dresselhaus, L.G. Cançado, A. Jorio, R. Saito, Studying disorder in graphite-based systems by Raman spectroscopy, Phys. Chem. Chem. Phys. 9 (2007) 1276–1290, https://doi.org/10.1039/B613962K.
[26] A. Merlen, J. Buijnsters, C. Pardanaud, A guide to and review of the use of multiwavelength Raman spectroscopy for characterizing defective aromatic carbon solids: from graphene to amorphous carbons, Coatings 7 (2017) 153, https://doi.org/10.3390/coatings7100153.
[27] A.C. Ferrari, J. Robertson, Interpretation of Raman spectra of disordered and amorphous carbon, Phys. Rev. B 61 (2000) 14095–14107, https://doi.org/10.1103/PhysRevB.61.14095.
[28] C. Castiglioni, F. Negri, M. Rigolio, G. Zerbi, Raman activation in disordered graphites of the A1′ symmetry forbidden k≠0 phonon: the origin of the D line, J. Chem. Phys. 115 (2001) 3769–3778, https://doi.org/10.1063/1.1381529.
[29] V. Zólyomi, J. Koltai, J. Kürti, Resonance Raman spectroscopy of graphite and graphene, Phys. Status Solidi B 248 (2011) 2435–2444, https://doi.org/10.1002/pssb.201100295.
[30] B.S. Elman, M.S. Dresselhaus, G. Dresselhaus, E.W. Maby, H. Mazurek, Raman scattering from ion-implanted graphite, Phys. Rev. B 24 (1981) 1027–1034, https://doi.org/10.1103/PhysRevB.24.1027.
[31] T. Livneh, T.L. Haslett, M. Moskovits, Distinguishing disorder-induced bands from allowed Raman bands in graphite, Phys. Rev. B 66 (2002) 195110, https://doi.org/10.1103/PhysRevB.66.195110.
[32] A.C. Ferrari, Raman spectroscopy of graphene and graphite: disorder, electron–phonon coupling, doping and nonadiabatic effects, Solid State Commun. 143 (2007) 47–57, https://doi.org/10.1016/j.ssc.2007.03.052.
[33] L.G. Cançado, A. Jorio, E.H.M. Ferreira, F. Stavale, C.A. Achete, R.B. Capaz, M.V. O. Moutinho, A. Lombardo, T.S. Kulmala, A.C. Ferrari, Quantifying defects in graphene via Raman spectroscopy at different excitation energies, Nano Lett. 11 (2011) 3190–3196, https://doi.org/10.1021/nl201432g.
[34] E.H. Martins Ferreira, M.V.O. Moutinho, F. Stavale, M.M. Lucchese, R.B. Capaz, C. A. Achete, A. Jorio, Evolution of the Raman spectra from single-, few-, and many-layer graphene with increasing disorder, Phys. Rev. B 82 (2010) 125429, https://doi.org/10.1103/PhysRevB.82.125429.
[35] L.G. Cançado, K. Takai, T. Enoki, M. Endo, Y.A. Kim, H. Mizusaki, A. Jorio, L. N. Coelho, R. Magalhães-Paniago, M.A. Pimenta, General equation for the determination of the crystallite size La of nanographite by Raman spectroscopy, Appl. Phys. Lett. 88 (2006) 163106, https://doi.org/10.1063/1.2196057.
[36] H.O. Pierson, Handbook of Carbon, Graphite, Diamond and Fullerenes : Properties, Processing and Applications, Noyes Publications, 1995.
[37] C.G. Zoski (Ed.), Handbook of Electrochemistry, first ed., Elsevier, Amsterdam ; Boston, 2007.
[38] J.E. O'Reilly, Oxidation-reduction potential of the ferro-ferricyanide system in buffer solutions, Biochim. Biophys. Acta BBA - Bioenerg. 292 (1973) 509–515, https://doi.org/10.1016/0005-2728(73)90001-7.
[39] S. Maass, F. Finsterwalder, G. Frank, R. Hartmann, C. Merten, Carbon support oxidation in PEM fuel cell cathodes, J. Power Sources 176 (2008) 444–451, https://doi.org/10.1016/j.jpowsour.2007.08.053.
[40] A. García-Miranda Ferrari, C.W. Foster, P.J. Kelly, D.A.C. Brownson, C.E. Banks, Determination of the electrochemical area of screen-printed electrochemical sensing platforms, Biosensors 8 (2018) 53, https://doi.org/10.3390/bios8020053.
[41] M.G. Trachioti, A.Ch Lazanas, M.I. Prodromidis, Shedding light on the calculation of electrode electroactive area and heterogeneous electron transfer rate constants at graphite screen-printed electrodes, Microchim. Acta 190 (2023) 251, https://doi.org/10.1007/s00604-023-05832-w.
[42] S.J. Konopka, Bruce McDuffie, Diffusion coefficients of ferri- and ferrocyanide ions in aqueous media, using twin-electrode thin-layer electrochemistry, Anal. Chem. 42 (1970) 1741–1746, https://doi.org/10.1021/ac50160a042.
[43] R.S. Nicholson, Theory and application of cyclic voltammetry for measurement of electrode reaction kinetics, Anal. Chem. 37 (1965) 1351–1355, https://doi.org/10.1021/ac60230a016.
[44] K. Grennan, A.J. Killard, M.R. Smyth, Physical characterizations of a screen-printed electrode for use in an amperometric biosensor system, Electroanalysis 13 (2001) 745–750, https://doi.org/10.1002/1521-4109(200105)13:8/9<745::AID-ELAN745>3.0.CO;2-B.

[45] M. Šadl, B. Repič, I. Goričan, D. Kuščer, H. Uršič, Aerosol-deposition derived graphite thick films for electrochemical sensors, Inf. MIDEM 54 (2024), https://doi.org/10.33180/InfMIDEM2024.302.
[46] F. Bottari, G. Moro, N. Sleegers, A. Florea, T. Cowen, S. Piletsky, A.L.N. van Nuijs, K. De Wael, Electropolymerized o-phenylenediamine on graphite promoting the electrochemical detection of nafcillin, Electroanalysis 32 (2020) 135–141, https://doi.org/10.1002/elan.201900397.
[47] A. Molina, E. Laborda, J. González, R.G. Compton, Effects of convergent diffusion and charge transfer kinetics on the diffusion layer thickness of spherical micro- and nanoelectrodes, Phys. Chem. Chem. Phys. 15 (2013) 7106, https://doi.org/10.1039/c3cp50290b.